

UKAEA-CCFE-PR(20)69

M.R. Gilbert, L.W. Packer, T. Stainer

Experimental validation of inventory simulations on molybdenum and its isotopes for fusion applications

Enquiries about copyright and reproduction should in the first instance be addressed to the UKAEA Publications Officer, Culham Science Centre, Building K1/O/83 Abingdon, Oxfordshire, OX14 3DB, UK. The United Kingdom Atomic Energy Authority is the copyright holder.

The contents of this document and all other UKAEA Preprints, Reports and Conference Papers are available to view online free at scientific-publications.ukaea.uk/

Experimental validation of inventory simulations on molybdenum and its isotopes for fusion applications

M.R. Gilbert, L.W. Packer, T. Stainer

Experimental validation of inventory simulations on molybdenum and its isotopes for fusion applications

M.R. Gilbert, L.W. Packer and T. Stainer

Culham Centre for Fusion Energy, UKAEA, Culham Science Centre, Abingdon, OX14 3DB, UK

E-mail: mark.gilbert@ukaea.uk

Abstract. Molybdenum is a potential material for future nuclear fusion experiments and power plants. It has good thermo-mechanical properties and can be readily fabricated, making it attractive as an alternative material to tungsten (the current leading candidate) for high neutron flux and high thermal load regions of fusion devices. Unfortunately, exposure to those fusion neutrons is predicted to cause significant long-term radioactivity in elemental Mo, which would be a problem during maintenance and decommissioning operations. Simulation predictions indicate that Mo activation could be reduced by isotopic adjustment (biasing). If these predictions are proven, then Mo could be used in future demonstration and commercial reactors without significantly increasing the amount of long-term, higher-level radioactive waste.

Transmutation (inventory) simulations used to predict activation rely on nuclear reaction data. The quality of these data impact on the confidence and uncertainty associated with predictions. Recently, UKAEA has developed benchmarks to test and validate the FISPACT-II inventory code and the input nuclear data libraries. Verification of molybdenum inventory simulations is performed against experimental decay-heat measurements from JAEA's fusion neutron source (FNS) facility and using new data acquired from γ -spectroscopy measurements of Mo irradiated in the ASP 14 MeV facility in the UK.

Results demonstrate that FISPACT-II predictions (with TENDL libraries) for Mo are accurate for activity generated from the shorter-lived radionuclides explored by these laboratory experiments. However, these kinds of experiments are limited in their coverage of the important radionuclides and decay timescales, and thus further experiments with fusion relevant operational scenarios and alternative measurement techniques are still needed.

Keywords: Molybdenum, fusion environment, experimental validation, nuclear reactions, 14 MeV neutrons, isotopic tailoring

1. Introduction: Molybdenum as a fusion material

Molybdenum (Mo) is often proposed as an alternative material for the high neutron flux and high thermal load regions – the plasma-facing components (PFCs) – of nuclear fusion devices [1, 2]. While tungsten (W) is the main candidate [3, 4], difficulties with fabrication and issues surrounding irradiation-induced embrittlement [3] lead to continued interest in alternatives, such as Mo. Mo exhibits similarly low sputtering yields [1] and equivalent thermal-mechanical properties to tungsten (including similar thermal conductivity – around 140 and 170 W m⁻¹ K⁻¹ for Mo and W, respectively), while being potentially easier to fabricate (at room temperature) into fusion components [5, 6].

Aside from a straight replacement for W, Mo is also an ideal candidate as an interlayer between W and a substrate such as carbon (C) – for example in the first wall armour tiles of the divertor [7, 8] – because it has a good match with the thermal expansion coefficients of both W and C [6]. Mo and its alloys, particularly with rhenium (Re), also have a high strength and resistance to radiation swelling [9], and were once widely considered for the heat-sink of early divertor concepts for ITER (for example, see [9, 10]). However, a key drawback for Mo as a fusion material concerns its induced radioactivity (and dose [2]) under neutron irradiation, which would likely prevent its widespread use (in its natural abundance isotopic form) due to the additional challenges associated with disposal of fusion waste and the associated maintenance of highly activated components.

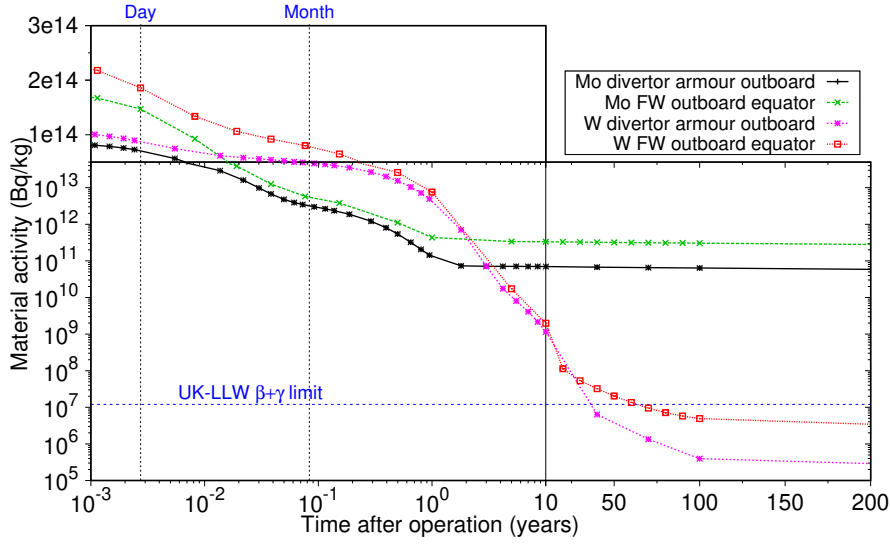
1.1. Activation in EU-DEMO

For tungsten, the predicted radiological response is not too severe at long decay (cooling) times, although impurities introduced during the manufacture of industrial W, such as cobalt (Co) and potassium (K) at concentrations of around 0.001 weight % [11], could create a waste problem [12]. At short times (weeks, months, or even several years), W-based components of a fusion reactor (particularly the divertor) will require active cooling even after operation as significant residual decay heat will be generated by β -emitting radionuclides: ¹⁸⁵W ($T_{1/2} \approx 75$ days) and ¹⁸⁷W (~ 24 hours) [13, 11].

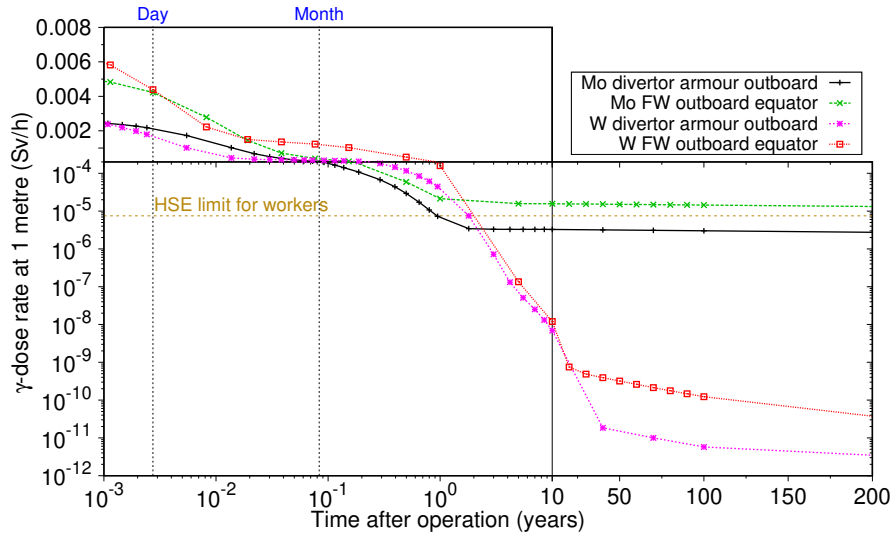
Conversely, short-term activity is less of an issue for Mo; decay-heat and activity from Mo is predicted to be lower than in W after a typical fusion first wall exposure and around two-orders of magnitude lower after a year [14], which is confirmed by the calculations below (see Figure 1). However, at longer timescales – decades and beyond – several problematic radionuclides are predicted to remain in naturally occurring Mo at levels sufficient to exceed regulatory limits for low-level waste (LLW) disposal. This makes it difficult to justify pure Mo for fusion applications where the goal is to avoid the generation of higher-level waste requiring long-term deep geological disposal [12].

For example, if Mo were used instead of W for divertor PFCs (armour), or in the tritium-breeder-blanket first-wall armour, of the latest design concepts for a European demonstration power plant (DEMO) then, after typical operating scenarios for that device, “natural” Mo is predicted to exceed the 12 MBq kg⁻¹ $\beta+\gamma$ emissions limit [15] for disposal in the UK’s low-level, near-surface waste repositories for more than 1000 years. Here natural refers to Mo composed of its stable isotopes in their naturally occurring concentrations (⁹²Mo: 14.65%, ⁹⁴Mo: 9.19%, ⁹⁵Mo: 15.87%, ⁹⁶Mo: 16.67%, ⁹⁷Mo: 9.58%, ⁹⁸Mo: 24.29%, ¹⁰⁰Mo: 9.74%). This prediction is based on the results

in figure 1(a), which shows the time-evolution in activation of irradiated Mo after the expected operational lifetime of divertor and blanket components in DEMO.



(a)



(b)

Figure 1. Colour online. Simulation results for predicted post-operation activity of Mo and W (both with naturally occurring isotopic abundances) after typical fusion DEMO reactor exposures in the first wall (FW) of the blanket and in the armour tiles of the divertor. The post-operation activity in Bq/kg (a) and γ dose-rate at 1 m in Sv/h (b) is shown as a function of time for natural Mo and W after typical component lifetimes. See the main text for details.

For this calculation, neutron flux-energy spectra were computed using Monte Carlo neutron-transport simulations (with MCNP [16]) for the 2015 DEMO

baseline [17] design with a Helium-Cooled tritium breeding blanket made from a Pebble-Bed of beryllium and lithium-orthosilicate (abbreviated as HCPB; see [18] for details). Figure 2 shows the neutron flux spectra obtained from those calculations for the two reactor locations considered here. Note that W was the armour material in these MCNP simulations; the spectra have the deep flux depressions associated the giant neutron-capture resonances of W in the 1-100 eV energy range – a phenomenon known as self-shielding [19, 20].

It is always advisable to perform neutron-transport simulations with the correct material compositions in the geometry. However, for the purposes of the present work, where the focus is on a comparison of the radiological response of W and Mo, MCNP simulations have not been repeated with Mo as the armour material. For the thin armour layers where these spectra were recorded (2 and 5 mm thick for the armour of the blanket first wall and divertor, respectively), the main influence on the spectral shape and total flux comes from the bulk materials behind them: structural steels, coolant, and function materials. Previous work (the activity analysis associated with [20]) demonstrated that, while subtle changes in the neutron spectrum caused by material variation can have significant impact on transmutation (composition change), the effect on activity is less profound and certainly not significant compared to the logarithmic variations shown in figure 1.

The two neutron spectra (one for the blanket and one for the divertor) were used in calculations performed with the FISPACT-II [21] inventory code; an inventory code predicts the time evolution of material compositions (from which the radiological response can be derived) using numerical solutions to the set of differential equations governing the rate-of-change of each nuclide in the system due to neutron irradiation and decay [21]. FISPACT-II was used with TENDL-2017 [22] nuclear data to predict the material response to either ~ 5 years (for the divertor outboard target armour) or ~ 15 years (outboard equatorial blanket first wall armour) of pulsed operation; these are typical scenarios planned for DEMO, where the divertor is expected to be replaced every 5 years and the second phase of DEMO will use as single blanket for its entire 15-year campaign [11, 23]. Subsequently, FISPACT-II time-evolution was continued to track the post-operational decay activity and γ dose-rate. Note that corrections for the capture-resonances, via probability tables, were included in the simulations for both Mo and W – see [20, 21] for details.

Figure 1(a) includes equivalent results for natural W in the two reactor regions considered and the difference compared to Mo is dramatic; W comfortably meets the UK $\beta+\gamma$ -activity limit for LLW (shown in the plot as a horizontal line) in both the divertor and blanket armour cases on a reasonable 30-100 year timescale, while Mo exceeds it by several orders of magnitude even after 1000 years. Note that UK-LLW also has an α limit, but this is not relevant here as neither Mo or W produce α -emitting radionuclides under neutron irradiation.

Similarly, the γ dose-rate from Mo is predicted to be many orders of magnitude higher than that from W from 10-years after the operational life of blanket and divertor components in DEMO. Figure 1(b) charts the time-evolution in γ dose-rate, in units of Sv/h, from an idealised 1 g “point source” of either Mo or W – this approximation of dose calculated by FISPACT-II is more conservative (lower) than the alternative, default “contact” dose approximation and is more relevant for radiation workers working in a nuclear environment and wearing protective clothing (a full γ -transport simulation is required for a more reliable prediction of γ -dose, see for example [25]). The UK’s Health and Safety Executive (HSE) recommends, based

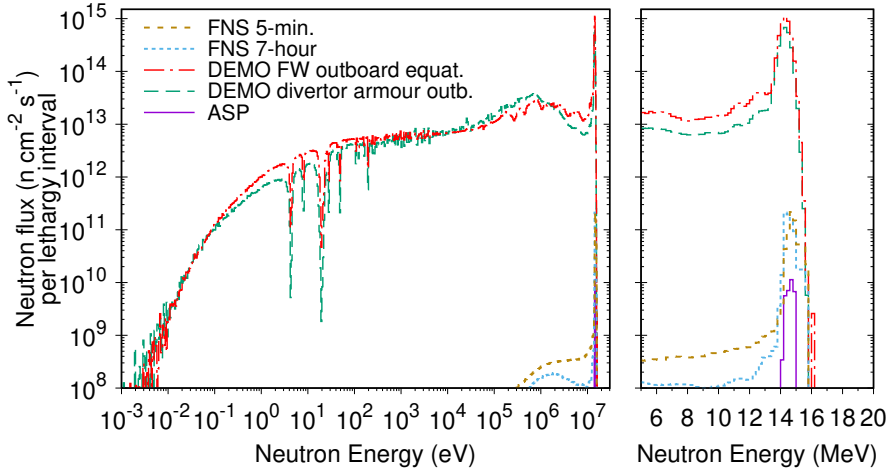


Figure 2. Colour online. Simulated neutron spectra for the two different DEMO reactor locations discussed in the main text, as well as for the conditions experienced by the thin, $25 \times 25 \text{ mm}^2$ Mo samples in the FNS experiments, and the ASP spectrum calculated in [24] and used to irradiate Mo foils. See the main text for details.

on the UK's regulations for ionising radiation [26], a limit of $7.5 \mu\text{Sv/h}$ (shown in the plot as a horizontal dashed line) for areas where workers will be exposed to ionising radiation [27]. While W, meets this limit within a year of post-operation cooling, the results show that Mo might pose a problem – while the dose-rate predictions for Mo in the divertor falls below the limit with a year, the dose-rate from Mo in the armour of the blanket remains above it for 100s of years. Even the divertor result remains close to this limit (and thus still potentially presenting a handling and maintenance problem, especially if manufacturing impurities were taken into account [12]), while the dose-rate from W is predicted to fall below 1 nSv/h within 10 years.

1.2. Radioisotope contributions to Mo activity

Figure 3 illustrates the reasons behind the long-term high activity (and γ dose) in Mo; it shows the time-evolution after operation in individual activity (and γ dose) contributions from the different radionuclides (or radioisotopes) produced in Mo during the FISPACT-II simulation of 5-years in a divertor armour tile. The absolute activities (figure 3(a)) show that five radionuclides are each produced in sufficient quantities for their respective absolute activities to exceed the UK-LLW – four with half-lives of more than 500 years and a fifth, ^{93m}Nb , with a relatively short half-life, but whose concentration is in secular equilibrium with the long-lived ^{93}Mo that decays to it (see table 1), which is why their respective activities are identical. On the other hand, although Mo is much closer to the limit than W (figure 1(b)), it does not exceed the HSE γ -dose rate limit beyond around 1 year after operation (figure 3(c)) in these simulation, and thus neither do the dose contributions from those individual radionuclides (or any other).

The highest activation (and dose) contribution at these long decay times comes from ^{91}Nb , which, in this simulation for the divertor armour, contributes between 60 and 80% of the activity (and dose) at all decay times greater than 2 years and

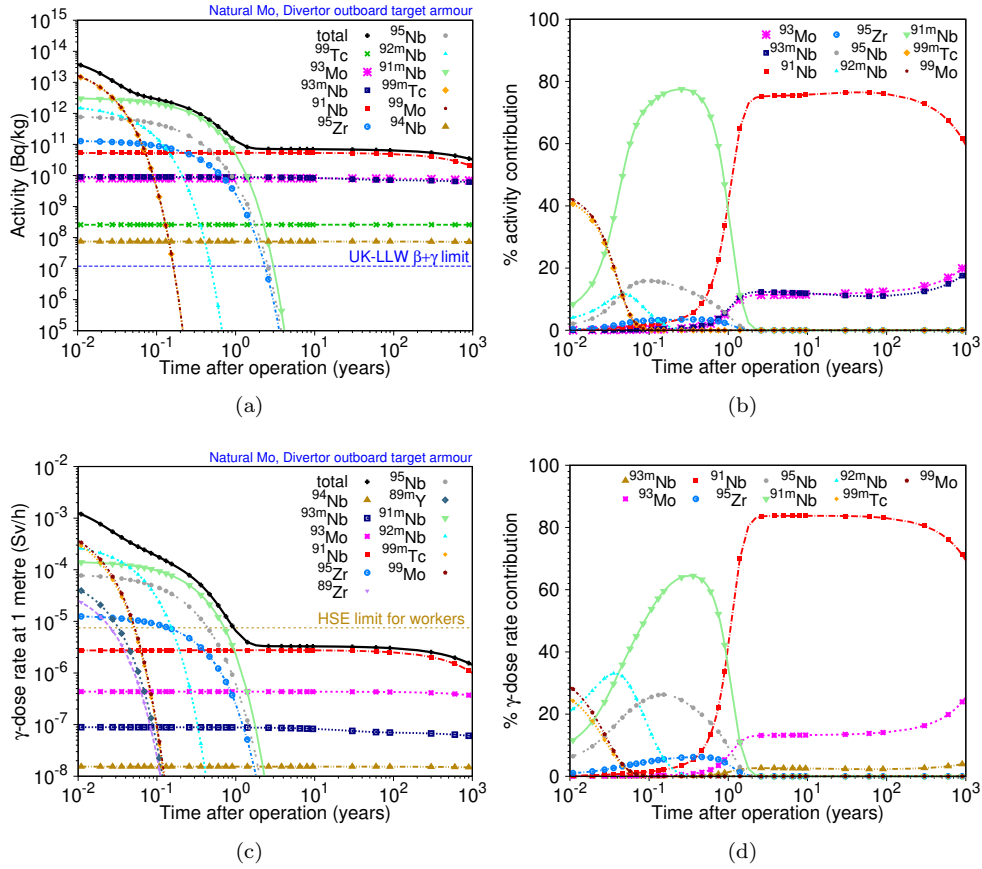


Figure 3. Colour online. Radionuclide contribution curves to the activity and γ -dose in Mo predicted after a ~ 5 -year exposure to the divertor armour spectra (figure 2). (a) absolute activities, (b) % activity contributions, (c) absolute γ -dose rates, and (d) % dose contributions. See the main text for details.

less than 1000 years (the limit of the simulations in this case) – as shown in by the % activity (dose) contribution evolution curves (described in [28]) of the same simulation in figure 3(b) (and 3(d) for dose).

The reaction pathways to produce these five nuclides from natural Mo and the relative (%) production contribution of those pathways were automatically calculated by FISPACT-II during the irradiation simulation (a unique feature of the code [21]) and these are shown in table 1. Pathways for three shorter-lived nuclides – ^{99m}Tc, ⁹⁹Mo and ^{91m}Nb – that contribute at least 40% to the total activity during decay times of less than 1 year (see figure 3(b)) are also included for reference (and are relevant for the experimental validation discussed later). Comparing these reaction chains to the isotopic abundance distribution of Mo (given earlier) we can see that not all of Mo stable isotopes are involved in the production of these problem radionuclides. In particular, neither ⁹⁶Mo or ⁹⁷Mo appear in the table at all, and, moreover, the radionuclides with the three highest contributions to long-term activity in figure 3 – ⁹³Mo, ^{93m}Nb and ⁹¹Nb – are produced almost entirely by reaction pathways from the

two lightest stable isotopes of Mo; ^{92}Mo and ^{94}Mo .

Table 1. Table showing the primary generation pathways for the important radionuclides generated in natural Mo during exposure to the operating conditions expected for the outboard divertor armour of a typical DEMO concept. For each nuclide, the % contribution for each path corresponds to the results computed by FISPACT-II using TENDL-2017 nuclear data. Pathways here and in subsequent tables were identified using the tree-search algorithm employed in FISPACT-II, invoked via the UNCERT and LOOKAHEAD keywords – see [29] for more details.

Product	$T_{1/2}$	Pathways	Path %
^{99m}Tc	6.0 hours	$^{98}\text{Mo}(n,\gamma)^{99}\text{Mo}(\beta^-)^{99m}\text{Tc}$	55.4
		$^{100}\text{Mo}(n,2n)^{99}\text{Mo}(\beta^-)^{99m}\text{Tc}$	44.5
^{99}Mo	2.7 days	$^{98}\text{Mo}(n,\gamma)^{99}\text{Mo}$	55.4
		$^{100}\text{Mo}(n,2n)^{99}\text{Mo}$	44.5
^{91m}Nb	61 days	$^{92}\text{Mo}(n,np)^{91m}\text{Nb}$	94.5
^{93m}Nb	16 years	$^{94}\text{Mo}(n,np)^{93m}\text{Nb}$	68.2
		$^{94}\text{Mo}(n,d)^{93m}\text{Nb}$	21.3
		$^{94}\text{Mo}(n,2n)^{93}\text{Mo}(\beta^+)^{93m}\text{Nb}$	6.3
^{91}Nb	680 years	$^{92}\text{Mo}(n,np)^{91}\text{Nb}$	84.9 ^a
		$^{92}\text{Mo}(n,2n)^{91}\text{Mo}(\beta^+)^{91}\text{Nb}$	14.2
^{93}Mo	3500 years	$^{92}\text{Mo}(n,\gamma)^{93}\text{Mo}$	22.0
		$^{94}\text{Mo}(n,2n)^{93}\text{Mo}$	77.5
^{94}Nb	20000 years	$^{94}\text{Mo}(n,p)^{94}\text{Nb}(\beta^-)^{94}\text{Nb}$	75.3 ^c
		$^{95}\text{Mo}(n,np)^{94}\text{Nb}$	24.2 ^c
^{99}Tc	210000 years	$^{98}\text{Mo}(n,\gamma)^{99}\text{Mo}(\beta^-)^{99}\text{Tc}$	55.4 ^b
		$^{100}\text{Mo}(n,2n)^{99}\text{Mo}(\beta^-)^{99}\text{Tc}$	44.5 ^b

^aincludes contribution from the production (via the same path as the ground-state) and subsequent decay of ^{91m}Nb .

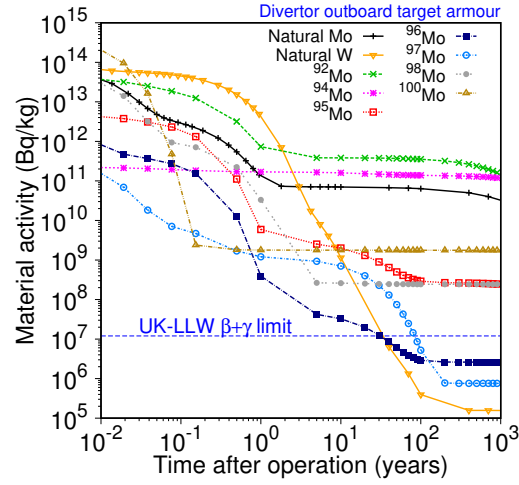
^bincludes contribution from the production and decay of ^{99m}Tc .

^cincludes contribution from the production and decay of ^{94m}Nb , $T_{1/2} = 6.3$ minutes.

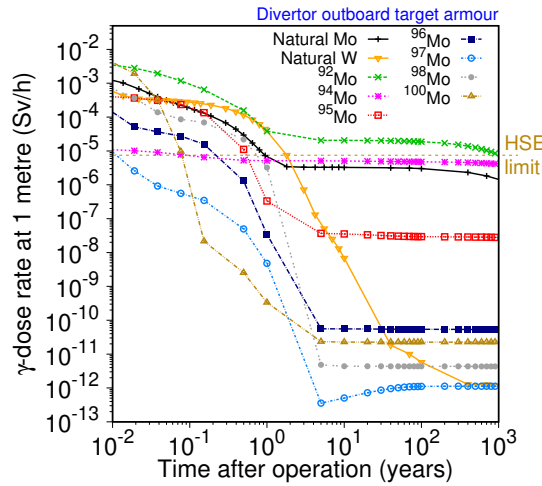
1.3. Activation of individual Mo isotopes

This observation – that only some of the stable Mo isotopes cause high activation in Mo – is confirmed by the inventory simulation results of decay-activity and γ dose in figure 4, where each Mo isotope has been separately exposed to the same DEMO divertor scenario as natural Mo, whose decay curve is also shown in the plots (as is natural W). As expected from the pathway analysis (table 1), ^{92}Mo and ^{94}Mo generate even higher activity levels (figure 4(a)) at long decay times than natural Mo because of the relative increase in production of the main problematic radionuclides discussed above. Meanwhile, the activity from mono-isotopic Mo (the feasibility of this is discussed below) composed of either ^{96}Mo or ^{97}Mo would actually satisfy UK-LLW limits on the desirable sub-100-year timescale in this DEMO scenario. Simulations for the remaining three isotopes (A=95,98,100) predict activities above the LLW limit

beyond 1000 years, but their activities are still 1–2 orders of magnitude below ^{92}Mo , ^{94}Mo and hence natural Mo.



(a)



(b)

Figure 4. Colour online. Simulation results Mo isotopes after a ~ 5 -year exposure to the divertor armour spectra (figure 2). The post-operation activity in Bq/kg (a) and γ dose-rate at 1 m in Sv/h (b) is shown as a function of time for different stable isotopes of Mo that have been individually exposed to a lifetime scenario for the outboard divertor target armour of DEMO (results for naturally occurring Mo and W are also shown for comparison). See the main text for details. Notice the slight increase in γ -dose rate in ^{97}Mo from around 4 years after operation, which is due to the feeding of ^{93m}Nb ($T_{1/2}=16$ years) from the decay of the long-lived ^{93}Zr ($T_{1/2} = 1.5 \times 10^6$ years).

The authors have previously [2] demonstrated a similar favourable result for ^{96}Mo or ^{97}Mo from the perspective of contact γ -dose rate, which is confirmed by the present predictions for γ dose at 1 m shown in figure 4(b) for the individual stable isotopes of

Mo. As in [2], also note that ^{98}Mo and ^{100}Mo have relatively low γ dose-rate beyond 10-years of cooling because the main long-lived radionuclide produced in them, ^{99}Tc (see table 1) is not a γ -emitter.

1.4. Isotopic tailoring of Mo: a solution for fusion?

The results above suggest a solution that could make Mo more viable for fusion applications – instead of natural Mo, use Mo with an artificially adjusted (tailored) distribution of stable isotopes, preferably dominated by ^{96}Mo and ^{97}Mo . A number of different technological possibilities exist for isotopic enrichment; enrichment via cascades in gas centrifuges [30], and via a free electron laser of CO_2 [31] has been explored for Mo, while electromagnetic separation [32, 33] is potentially a viable approach to achieve high enrichment of the middle mass range of Mo isotopes (*i.e.* the ones that would produce low activation Mo) and is the only viable method for isotope separation of many elements, including rare-earth metals [32]. However, it is recognised that the (likely) high cost of using several tonnes of isotopically enriched Mo as a first wall material in a fusion reactor would have to be balanced against the potential benefit – e.g. of having reduced economic and environmental costs for waste disposal.

Alternatively, Mo with a modified isotope distribution could be useful to reduce the activation of fusion alloys, such as the ferritic-martensitic steels needed for in-vessel reactor components. For example, previous work [34] suggests that using tailored Mo in EUROFER steel might be a reasonably economic solution to reduce maintenance requirements and improve thermodynamic efficiency.

Mo is also touted as having potential applications as a structural material in fuel elements to improve safety in future generations of fission power plants [30, 35]. In this case, the barrier to realisation is the very high (thermal) capture cross section for neutrons in natural Mo, which is obviously undesirable when trying to create a sustained nuclear reaction. Once again, isotopic tailoring to reduce the problematic isotopes (in this case mainly ^{95}Mo , which has a capture cross section of 13.6 barns at a neutron energy of 0.025 eV [35]) offers a possible solution.

Excessively high neutron capture cross sections could also be a problem for fusion, although in that case, molybdenum’s potential application in fusion PFCs would not be concerned with thermal neutron capture as such locations in a reactor are overwhelmingly dominated by fast, 14 MeV neutrons (*i.e.* the neutron energies generated as a result of the deuterium-tritium [DT] fusion reaction). However, it could be a concern if Mo is used in significant concentrations in the tritium-breeding zone, where the loss of neutrons in a material with a high absorption cross section could impact on the TBR (tritium breeding ratio) [36]. This might impact more severely breeding blanket concepts involving Li-Pb eutectic where satisfactory tritium breeding rates are reliant on high ^6Li enrichment (around 90% [11]). The $^6\text{Li}(n,\alpha)^3\text{H}$ cross section is particularly high at low neutron energies and competing capture

Notice that in the divertor simulations (figure 4(a)) activity levels of pure ^{96}Mo or ^{97}Mo are relatively (compared to the much higher activity from other pure isotopes) close to the UK-LLW limit. Indeed, in the other case from figure 1(a), for the blanket first wall armour, even for these two isotopes the generated long-term activity (typically from longer reaction chains involving neutron multiplication, (n,2n) and/or neutron capture reactions to the same radionuclides shown in table 1) would exceed the LLW limit. Thus isotopic tailoring is unlikely to be a complete solution for the

waste disposal of fusion components containing Mo (unless regulatory limits can be revised/relaxed for fusion waste [12]). However, isotopically adjusted Mo could be used in a “mixed solution” with W, where W is used primarily in higher-flux first wall regions and therefore replaced more regularly, while Mo could be used as an armour in less exposed regions (e.g. in the divertor or away from the equator regions of the blanket), thus reducing the frequency with which those components need replacement (assuming Mo proved to be more resilient than W) and thereby reducing maintenance cycles and costs, and improving overall fusion plant availability.

Predictions such as those discussed in this introduction rely on accurate nuclear code simulations. While the numerical techniques employed by inventory codes like FISPACT-II or neutron transport simulators like MCNP are well-established and validated (see e.g. [37, 38]), it is still the case that the quality and completeness of the underlying nuclear data strongly determines the reliability of predictions and the level of uncertainty; the latter could strongly influence the level of conservativeness in engineering limits, which could impact on cost, and so there is a strong incentive to reduce uncertainty. Of particular importance for simulating the radiological response of molybdenum (or any other material) under fusion conditions is the accuracy of the integrated reaction rates that govern the production of dominant radionuclides. The remainder of this paper describes efforts at UKAEA to test and validate the nuclear reaction data used with FISPACT-II for, by benchmarking simulations results against both historical experimental decay-heat measurements and newly acquired γ -spectroscopy data.

2. Fusion Decay-heat Benchmark

At the end of the last century, JAEA used their 14 MeV fusion neutron source (FNS) facility to perform experiments on small material samples. The objective of the experiments undertaken by Maekawa *et al* [39, 40, 41, 42, 43] was to provide decay-heat data relevant to fusion systems that could be used to test the quality of nuclear simulations. This wealth of carefully obtained data has been used to validate inventory code predictions in the last two decades, but it was a relatively arduous and error-prone process until UKAEA’s recent efforts [44] to construct a fully-automated simulation benchmark. A detailed description of the benchmark, including the experiments and the simulation approach with FISPACT-II, is provided in [44] and the most recent complete benchmark, covering more than 70 materials and focussing on validating FISPACT-II with the TENDL-2017 [22] library, has been compiled into an openly accessible report [45]. Here, the discussion is focussed on the comparison between simulations and the experimental measurements for Mo.

For Mo, thin metallic foil samples 25×25 mm² in area and approximately 10 μ m thick, were irradiated for either 5 minutes or for 7 hours at a fluxes of between 10^9 and 10^{10} n cm⁻² s⁻¹. The reported decay-heat results by Maekawa *et al* were scaled to a flux of 10^{10} n cm⁻² s⁻¹ using the aluminium monitor foils that were included in each experiment to calibrate the neutron fluence based on γ spectroscopy of ²⁴Na produced via ²⁷Al(n, α)²⁴Na (similarly to the approach taken for ASP and described in [46]). Figure 2 shows the typical neutron spectra experienced by the samples in the 5-minute and 7-hour cases (different sample locations and hence different spectra – the 5-minute experiments used a rapid extraction system and associated set-up, which was not used in the 7-hour cases).

Decay-heat measurements at various cooling times after irradiation were obtained

from a whole energy absorption spectrometer (WEAS), which detected both β^- and γ emissions with near 100% efficiency using a twin BGO scintillators arrangement and a centrally located sample position to produce close to 4π steradians counting geometry [47]. For the 5-minute experiments, the rapid extraction system allowed the first measurements to occur within 1 minute of the end of irradiation and further measurements were taken for a further 1 hour. In the 7-hour case the first measurements did not take place until nearly 15 hours after the irradiation, but measurements were repeated for up to 200 days, allowing the contributions from radionuclides with longer half-lives to be captured.

Figure 5 shows the decay-heat measurements (as points) obtained for the two sets of Mo experiments (an earlier set of 5-minute irradiations of Mo are not included here for brevity, but are considered in [45]). Figures 5a and 5b, for 5-minute and 7-hour (*i.e.* a full day of irradiation time at the FNS facility) irradiations, respectively, compare the experiments to FISPACT-II simulations (curves) of the total decay-heat performed with TENDL-2017 [22] nuclear data and several other major international nuclear libraries (see [44, 45] for details). In both cases there is very good agreement between the simulation and experiment, with C/E (calculated decay-heat divided by experimental measurement) values generally close to one, particularly with TENDL-2017, where C/E values lie in the range 0.97–1.01 for the 5-minute experiment and 0.9–1.4 in the 7-hour case [45].

In the 5-minute experiment the main radionuclide contribution to decay-heat is ^{91}Mo , produced via (n,2n) reactions on ^{92}Mo (see the pathway analysis for FNS in table 2), which contributes at least 70% of the simulated decay-heat throughout the 1-hour of experimental measurement time, as shown in the % contribution chart in the bottom panel of figure 5c. The upper panel of 5c shows the absolute nuclide contribution breakdown [28] and there are a number of other, minor radionuclides predicted by the simulations, which are not important to capture the decay-heat from Mo under these short irradiation, short cooling time conditions.

However, in the longer, 7-hour experiment, the nuclide breakdown from the TENDL-2017 simulation (figure 5d) suggests a much more complicated picture, with a number of different radionuclides providing significant contributions to the total decay-heat at different times during the ~ 200 days of cooling time where experimental measurements were recorded. In the first week of cooling ^{99}Mo dominates, but as this nuclide decays with a half-life of 14.5 minutes (see table 2), by around 20 days of cooling it is replaced by three unstable nuclides of niobium with longer, 10-60 day half-lives: ^{92m}Nb , ^{95}Nb , and ^{91m}Nb . This relatively complex radiological landscape is a very good match to the experimental measurements – as demonstrated by the absolute nuclide breakdown plot, where the combination of decay-curves for these four nuclides produces a very good match to the time-evolution profile of the experiment. Such close agreement to experiment in such a complex case demonstrates the efficacy of the FISPACT-II system, including the computational method, and confirms the validity of the underlying nuclear data.

The pathway analysis for these simulated experiments in table 2 shows the major production routes for the five important radionuclides for FNS experiments on Mo. The cross sections (primarily for 14 MeV neutrons – see figure 2) of a number of different non-elastic reactions, such as (n,2n) [neutron multiplication] and (n,p) [neutron capture, proton emission], on several isotopes of Mo are tested (and validated) by this experimental benchmark for Mo. Included in the validation are some reactions that are predicted to be important for the activation of Mo in a fusion reactor (compare

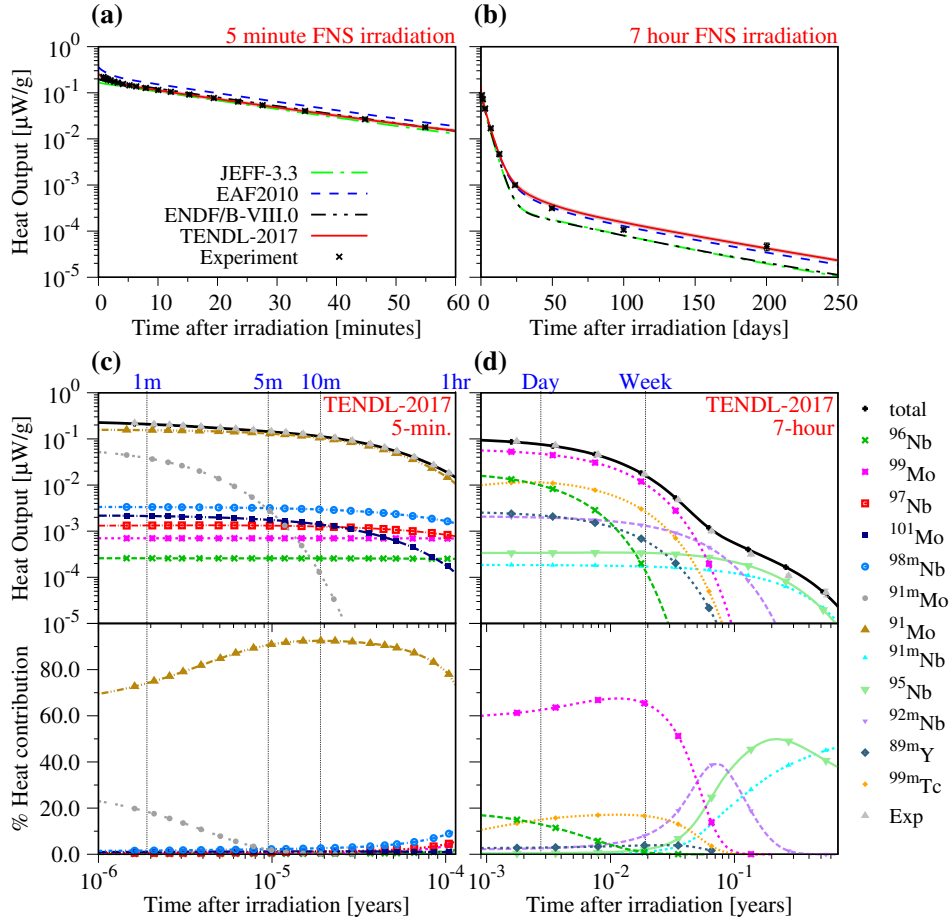


Figure 5. Colour online. Simulation & experimental decay-heat results from the FNS benchmark for molybdenum. (a) and (c) correspond to decay-heat following 5-minute irradiations, (b) and (d) are the equivalent data after 7-hour irradiations. (a) and (b) show total decay-heat curves on linear time-after-irradiation scales for the different nuclear library simulations with FISPACT-II, the experimental measurements as points with vertical lines showing experimental uncertainty, and the nuclear-data-uncertainty band (in grey) for the TENDL-2017 [22] library. (c) and (d) present the radionuclide breakdown of contributions to the total decay-heat from the TENDL-2017 simulations in absolute $\mu\text{W/g}$ terms (top halves) and as % contributions (bottom halves) – on logarithmic time-after-irradiation scales. See [44, 45] for more details.

tables 1 and 2), such as those producing ^{99}Mo and ^{91m}Nb . However, as expected, the experiments do not provide any useful data to test the production of the long-lived radionuclides that would cause disposal and handling problems for Mo components.

3. ASP Experiments

From 2011-2015 [48, 49, 50, 46, 51], in an effort to improve the quality of experimental reaction cross section data for fusion-relevant materials at fusion-relevant neutron

Table 2. List of contributing reaction-route pathways for the important radionuclides identified in FNS experiments. Full pathway analyses for each experimental simulation can be found in the main benchmark report [45].

Product	$T_{1/2}$	Relevant FNS experiment	Pathways	Path %
^{91}Mo	15.49 min.	5-min.	$^{92}\text{Mo}(n,2n)^{91}\text{Mo}$	100.0 ^a
^{99}Mo	2.7 days	7-hour	$^{100}\text{Mo}(n,2n)^{99}\text{Mo}$	99.6
^{92m}Nb	10 days	7-hour	$^{92}\text{Mo}(n,p)^{92m}\text{Nb}$	100.0
^{95}Nb	35 days	7-hour	$^{95}\text{Mo}(n,p)^{95}\text{Nb}$	83.2
			$^{96}\text{Mo}(n,d)^{95}\text{Nb}$	9.7
^{91m}Nb	61 days	7-hour	$^{92}\text{Mo}(n,np)^{91m}\text{Nb}$	92.3
			$^{92}\text{Mo}(n,d)^{91m}\text{Nb}$	3.9

^aincludes contribution from the production and isomeric transition (IT) decay of ^{91m}Mo , $T_{1/2} = 1.1$ min.

energies, UKAEA undertook a series of 14 MeV neutron irradiation experiments at the experimental facility known as ‘ASP’, which is hosted at AWE Aldermaston in the UK. The aim of the experimental campaigns was to gain additional cross section data-points at 14 MeV for reactions where data was deficient – this is true for many important reactions for fusion materials [52, 53] – and thus to aid the evaluators working on the next generation of nuclear data libraries by providing more information with which to fit the theoretical models that generate continuous cross section curves.

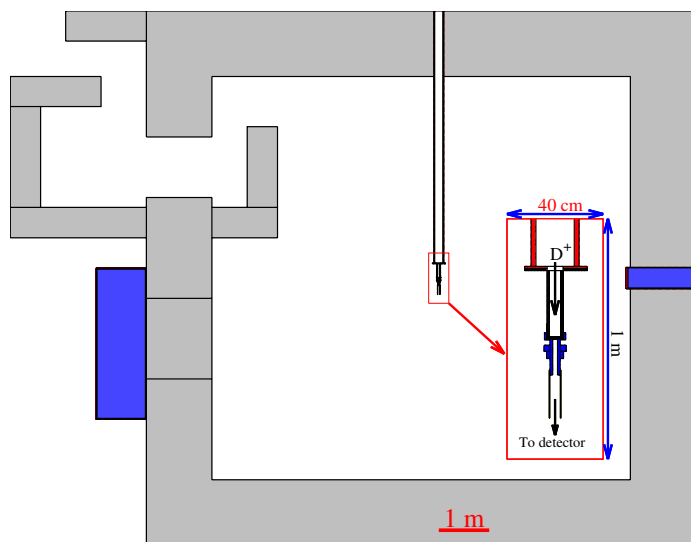


Figure 6. Colour online. Simplified ASP geometry (used in MCNP calculations) showing chamber walls and labyrinth exit (in grey) and a close up of the target geometry, where the incoming D^+ deuteron beam is accelerated onto the tritium target, which is adjacent to the sample chamber (in blue). Samples are inserted and extracted (to the γ detector) from this chamber via a pneumatic ‘Rabbit’ tube.

The experimental set-up involved an accelerated deuteron beam impinging onto a tritium-loaded target to produce a source of 14 MeV neutrons (via DT reactions), which was then used to irradiate a wide variety of material foils. After irradiation the foils were transferred rapidly via a pneumatic extraction “Rabbit” tube to a high-purity germanium (HPGe) γ -detector and the full time evolution in the energy-count profile of γ emissions from the activated material was recorded. Full details of the experimental approach are given in [48, 49]. So far, more than 300 separate experiments have been performed, generating more than 10000 separate γ spectra (the integral spectrum of γ counts is recorded at multiple time intervals for each experiment to enable analysis – see below), and previous efforts [46] to process such large data sets in a rigorous, consistent and automatic manner are still ongoing [24]. In the present work, we analyse eight experiments involving samples of Mo.

Figure 7 shows the typical raw data obtained from the ASP experiments, along with plots showing the different stages of the analysis approach. The data shown corresponds to experiment 82 in UKAEA’s campaign, which included a molybdenum foil. The full, time-integrated γ -spectrum (figure 7(a)) recorded for 15 minutes after irradiating the foil triplet of Mo-Fe-Al shows various peaks at characteristic γ -energies for different radionuclides produced in the foils during the ~ 5 -minute irradiation (both the irradiation time and measurement time varied between experiments, but was accurately recorded). The main peaks, which have an almost Gaussian profile, are centred on discrete γ emission lines and are highlighted in the figure, including the electron-positron annihilation peak at 511 keV, the potassium-40 (^{40}K) organic background signal at 1461 keV, and various peaks associated with radionuclides produced during irradiation in the Mo, Fe and Al foils.

Iron (Fe) and aluminium (Al) foils were included in the experiments to enable accurate measurement of the neutron fluence received at the sample location during irradiation [46]. In the present work, the major lines from ^{27}Mg at 844, 1014 and 171 keV, ^{24}Na lines at 1369 and 2754 keV due to aluminium activation, along with ^{56}Mn (produced in the Fe foil) lines at 847, 1811 and 2113 keV, were used to produce an average estimate of the neutron flux for each experiment. Note that for experiment 81, a transfer issue meant that the acquisition data (counts) from the aluminium foil were not properly recorded and so the flux estimate is based solely on the ^{56}Mn peaks in this case. Table 3 gives the details of the eight experiments considered here for Mo, including the results of the Fe/Al-foil flux estimates.

Ref. [46] exemplifies how the flux estimation was done using the Levenberg-Marquardt Algorithm (LMA – a damped least-squares method) to fit a decay function to the counts per (real) time (in seconds), and hence to calculate decay-corrected A_0 value in Bq corresponding to the end of irradiation activity. In calculating the flux using these reference foils, it is assumed that the reaction pathways (see table 4) to the measured nuclides are well-known and that the nuclear cross section data (from TENDL-2017 [22]) is well-validated. The cross section vector for each reaction is “folded” (vector dot product) with the ASP neutron irradiation spectra (calculated using a Monte Carlo simulation as part of the work described in [24] and shown in figure 2) to calculate the total cross section σ in barns. Using the standard decay equations describing the production and decay of radionuclides [54], A_0 , σ and the decay constant λ are used to estimate the experimental flux via:

$$\phi = \frac{A_0}{N\sigma(1 - \exp^{-t_{\text{irr}}\lambda})}, \quad (1)$$

where t_{irr} is the irradiation time of the experiment (given in table 3) and N is the total number of atoms of the target (stable) nuclide – in this case of ^{56}Fe or ^{27}Al . Note that this approach assumes that the flux is constant during the irradiation, which is a reasonably valid approximation in most experiments and was confirmed from inspection of the rates recorded by fission counters positioned near to the ASP target.

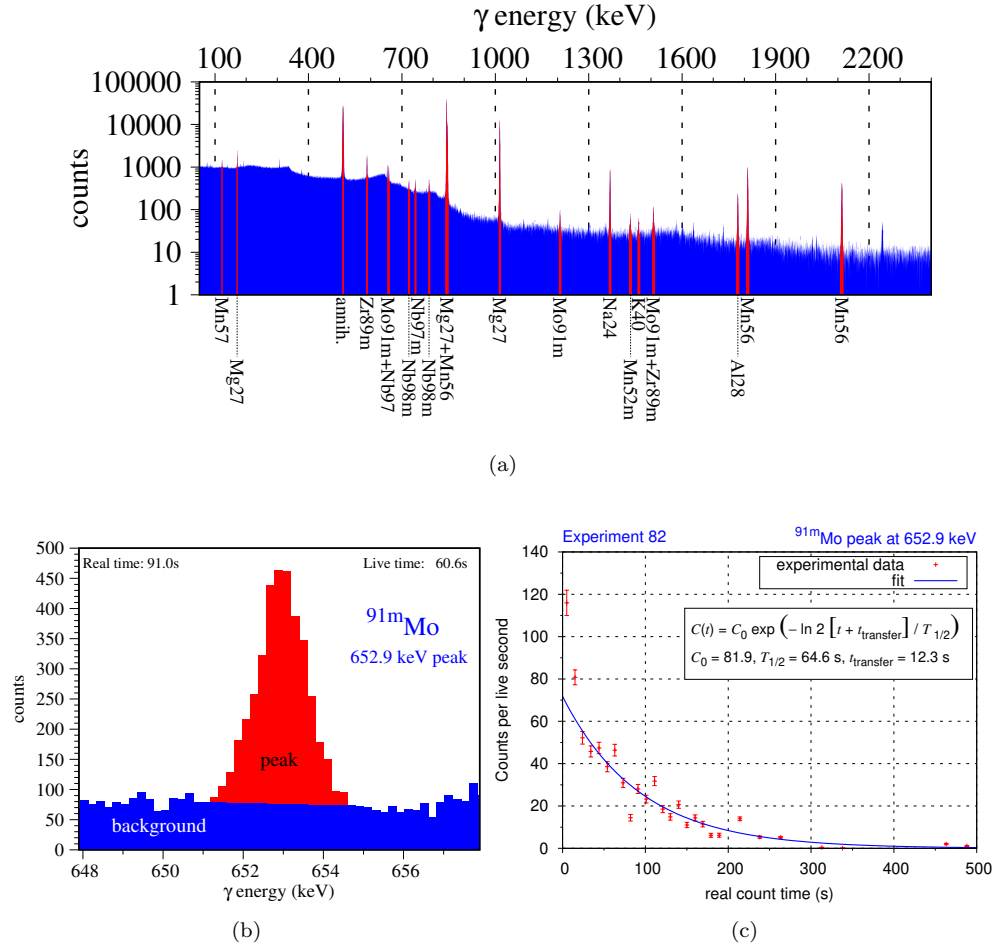


Figure 7. Colour online. Experiment 82 γ spectroscopy. (a): final (end of ~ 15 -min. acquisition) integrated γ spectrum. (b): 652.9 keV peak associated with $^{91\text{m}}\text{Mo}$ after 91 s, showing the peak area after subtraction of the background. (c): counts as a function of time for this peak and the curve fitted to the data (see main text for details). C_0 is the dependent (free) variable. t_{transfer} is the time delay between the end of the irradiation and the start of the γ -data acquisition – *i.e.* the transfer time.

The estimated fluxes are now used to both evaluate the experimental E activity of radionuclides in the molybdenum foils and also as input to FISPACT-II inventory simulations to obtain a calculated C activity. For the experimental value, the first stage is to extract the detector counts for each detectable γ -peak of the γ -emitting radionuclides produced during the irradiation of Mo at ASP. Peaks associated with five different radionuclides were identified in the present work; these are listed in table 4

Table 3. Experimental details and flux estimates for the ASP experiments involving Mo.

Experiment number	Material masses (g)			Irradiation time (min.)	Estimated flux ($\text{n cm}^{-2} \text{s}^{-1}$)
	Mo	Fe	Al		
81	0.1519	0.1066	N/A ^b	5	8.6×10^8
82	0.1529	0.1054	0.0382	5	9.3×10^8
111	0.1558	0.1063	0.0385	5	6.7×10^8
112	0.1551	0.1067	0.0389	4.67	6.8×10^8
134	0.4611 ^a	0.1062	0.0384	60	4.3×10^8
226	0.1539	0.1104	0.0362	10	2.5×10^8
244	0.1518	0.1105	0.0289	30	3.7×10^8
284	0.1537	0.1111	0.0293	30	8.6×10^8

^a three Mo foils were used in a stack for this longer irradiation experiment.

^b experimental issue, see main text for details.

(after the flux-estimator nuclides of Fe and Al), together with their half-lives, and main production pathways according to FISPACT-II simulations with TENDL-2017 for the irradiation time and flux-estimate associated with experiment 82 (see table 3). The identifiable peaks for each radionuclide are listed in table 4 and are labelled in the example complete spectrum for experiment 82 (figure 7(a)).

Figure 7(b) demonstrates the process by which the background counts (from Compton scattering) are subtracted, using linear interpolation between the average counts recorded in a range of channels on either side of a peak [46], to give the counts associated with the decaying nuclide – in this case for ^{91m}Mo associated with its γ line at 653 keV. The fit (using LMA, as before) to the resulting evolution in counts-per-live-second as a function of (real) time for a peak (e.g. as in figure 7(c) for the ^{91m}Mo peak) then gives the experimentally predicted count rate at the end of irradiation C_0 , which in turn is used to calculate A_0 via

$$A_0 = \frac{C_0}{D^{\text{eff}}(E_p^\gamma)I_p}, \quad (2)$$

where $D^{\text{eff}}(E^\gamma)$ is the detector efficiency at γ -energy E^γ , which for the HPGe detector used in the present work is described by a function fit to neutron transport simulations performed on a model of the detector (e.g. as described in [24]). E_p^γ and I_p are the energy and intensity of peak p , respectively, both taken from `decay_2012` decay-data files used by FISPACT-II [21] for TENDL-2017.

Meanwhile, the calculated (C) estimate of A_0 is taken directly from a FISPACT-II calculation with the TENDL-2017 data library. The appropriate mass of pure Mo was irradiated for the experimental irradiation time at the estimated flux (calculated as described above) and using the calculated neutron spectrum shown in figure 2 (the mass, flux-estimate, and irradiation times for each experiment are given in table 3). FISPACT-II automatically outputs the individual radionuclide contributions to the total sample activity, and the required end-of-irradiation values can be easily extracted for the specific nuclides. Thus calculated (C) and experimental (E) A_0 values are obtained for comparison.

Figure 8 shows all C/E values obtained from the eight Mo experiments. Note that C/E results for ^{97}Nb and ^{97m}Nb are plotted in the same pane, while the other three panes in the figure show results for single radionuclides (as labelled). The error

estimates on each value, shown as error bars in the figure, include the standard error of the flux estimate (*i.e.* the deviation of the flux values from the mean), the fractional error calculated by FISPACT-II and associated with the uncertainty data in TENDL (e.g. as shown in the grey error bands of the cross section figures in figure A1 of the appendix), and the standard statistical count uncertainty \sqrt{N}/N (from Poisson statistics and valid for sufficiently high enough counts) commonly applied to detector results. The errors have been summed in quadrature. Work is ongoing to refine these uncertainties and to account for other (potentially systematic) errors and correlations, such as those associated with the LMA fitting routine or from uncertainty in the experimental timing information, but the present estimates (potentially pessimistic) give an indication of the error magnitudes.

Note in figure 8 that not every experiment has produced a C/E value for every possible peak considered. Peaks with total background-corrected counts of less than 400 during the entire measurement time were deemed to be of low statistical quality and were omitted. Also shown for each pane is the weighted average C/E value, where the weights correspond to the inverse of the variance (square of the error) for each point. The standard deviation from these weighted averages is shown by the grey band in each plot.

The results for ^{89m}Zr are particularly good, with C/E near to one for almost all experiments. Only experiment 134 produces a discrepant result for this radionuclide – as it does for other nuclides considered – but this doesn't alter the overall agreement; as demonstrated by a weighted averaged C/E close to one and small spread of values about this mean. The irradiation time in this experiment was longer than usual for these experiments (see table 3) and the detector measurements were extended to an over-night count. The increased irradiation time, in particular, appears to have caused the peaks from the radionuclides of interest to have more background counts (potentially from Fe & Al) and thus lower overall counts than expected, leading to an underestimate from the experiment and high C/E results.

For ^{91m}Mo , *only* the lowest energy peak at 653 keV produces consistently good C/E values, which, at first, appears unexpected as the C values for a given experiment are identical for all peaks. 653 keV is the highest intensity peak ($I_p \approx 0.5$). The other, higher-energy peaks for this radionuclide have lower intensities and thus produce smaller count-rates in the experiments – the 653 keV peak integral typically comprised 2000-4000 counts for this nuclide, while the other two produced a maximum of around 700 counts each (some counts were even below the 400 threshold discussed above). This may explain the discrepancy observed in figure 8. On the other hand, figure A1(a) in the appendix, comparing the TENDL-2017 cross sections to the differential experimental data (*i.e.* cross sections values and single energies) available in the international EXFOR database [55] for the (n,2n) reaction that produces ^{91}Mo does suggest a slight overestimation for the path to the metastable 91m; the TENDL curve at 14 MeV is higher than the majority of the differential data. However, the result from the present work is not conclusive enough to make a recommendation for future TENDL evaluations.

Apart from experiment 134, for the reasons outlined above, C/E results for ^{98m}Nb are very good and relatively consistent for the two different peaks identified in the experiments, although there is a large spread between experiments and the weighted average is less than one.

Results for ^{97}Nb and ^{97m}Nb (one peak each) also show consistency within each experiment, but the calculated values appear to underestimate the production of these

two nuclides; the weighted average C/E is around 0.8 and the deviation from this mean does not include one. There is nothing conclusive in the comparison of TENDL-2017 to EXFOR in this case (figure A1(b)); if anything the TENDL cross sections for the primary (n,p) reaction (see table 4) producing ^{97}Nb appear to slightly underestimate the data at 14 MeV compared to EXFOR. The results for these nuclides need further investigation – probably involving additional experiments.

Generally, considering all of the experimental uncertainties, but particularly those associated with the flux estimation, the fact that many of the C/E values are close to one (and all are less than 2) is very encouraging and demonstrates that the FISPACT-II calculations with TENDL-2017 produce good predictions for irradiation-induced activity in Mo in these scenarios. However, it is worth observing that, in contrast to the FNS benchmark (section 2), none of the reaction pathways interrogated by these experiments are relevant for the dominant channels to long-lived isotopes identified in the earlier fusion power plant scenario (compare table 4 to table 1). Experiments involving measurement of such long-lived reaction products will likely require longer irradiations and post-irradiation measurements.

For these long-lived nuclides, including the important ^{91}Nb , ^{93}Mo , and ^{93m}Nb , the dominant production cross sections can have high uncertainty (e.g. the (n,np) channel responsible for the majority of ^{93m}Nb production has a nuclear data uncertainty greater than 50% in the TENDL-2017 [22] under the ASP neutron spectrum). This demonstrates the need for future experiments with careful design; *i.e.* to ensure that the important reaction pathways are explored and that the resulting benchmark is as relevant as possible for Mo in a fusion power plant.

4. Ongoing experimental need

Is it possible to measure the production cross sections for these longer-lived nuclides via experiment, particularly ^{91}Nb , ^{93}Mo , and ^{93m}Nb ? In general, one can envisage that in experimental campaigns aimed at these long-lived nuclides a large neutron fluence delivered over longer irradiation times (compared to those in the presented work, which focussed on short-lived isotopes) to expose large mass samples (in the 100s g region) will be required to generate a sufficiently high radiological signature from the isotopes to be able to measure them successfully. Such experiments, besides the small nuclear emission signal, would also initially exhibit a higher background-to-signal ratio due to the activity of the shorter-lived nuclides in the sample, making measurements potentially challenging in the first weeks and months after irradiation. For example, the FISPACT-II calculations in figure 3 illustrate that a cooling period of 1 year or more would be desirable to avoid taking measurements dominated by emissions from the shorter-lived nuclides ^{95}Zr , ^{91m}Nb , and ^{95}Nb . ^{95}Zr decays via β^- with a 64 day half-life and has a gamma emission mainly at 756.7 keV (with absolute intensity [probability] $I=0.544$) and 724.2 keV ($I=0.443$); ^{91m}Nb decays via isomeric transition (IT) with 60.9 day half-life and emits a γ -ray at 104.6 keV ($I=0.574$); ^{95}Nb also decays via β^- with key γ -emission at 765.8 keV ($I=0.998$) [56]. All these γ -signals could prohibit early measurement of some long-lived nuclides and would necessitate significantly extended post-irradiation measurement timescales.

Whilst ^{94}Nb is not a primary consideration here, it could be measured by gamma spectrometry. ^{94}Nb decays via β^- with a high probability ($I\approx 1.0$) γ -emission at 871.1 keV – an energy higher than those from the shorter-lived nuclides discussed above so would not adversely impact on a gamma-based ^{94}Nb measurement. On

Table 4. Information about the radionuclides measured in the ASP experiments. The FISPACT-II-calculated production pathways and their % contributions were obtained from the simulations with the TENDL-2017 library (see the main text). Only the γ -peak energies observed in the experiments are listed for each nuclide.

Product	$T_{1/2}$ experiment	Pathways	Path % TENDL-2017 (Exp. 82)	Experimentally Identifiable γ -peaks (keV)
^{56}Mn	2.58 hours	$^{56}\text{Fe}(\text{n,p})^{56}\text{Mn}$	100.0	846.8, 1810.7, 2113.1
^{27}Mg	9.46 min.	$^{27}\text{Al}(\text{n,p})^{27}\text{Mg}$	100.0	170.9, 843.7, 1014.4
^{24}Na	14.96 hours	$^{27}\text{Al}(\text{n},\alpha)^{24}\text{Na}$	100.0	1368.6, 2754.0
^{97m}Nb	53.0 s	$^{97}\text{Mo}(\text{n,p})^{97m}\text{Nb}$	83.7	743.4
		$^{98}\text{Mo}(\text{n,np})^{97m}\text{Nb}$	2.1	
		$^{98}\text{Mo}(\text{n,d})^{97m}\text{Nb}$	14.1	
^{91m}Mo	1.08 min.	$^{92}\text{Mo}(\text{n},2\text{n})^{91m}\text{Mo}$	100.0	652.9, 1208.1, 1508.0
^{89m}Zr	4.13 min.	$^{92}\text{Mo}(\text{n},\alpha)^{89m}\text{Zr}$	100.0	587.8
^{98m}Nb	51.30 min.	$^{98}\text{Mo}(\text{n,p})^{98m}\text{Nb}$	100.0	722.6, 787.4
^{97}Nb	1.23 hours	$^{97}\text{Mo}(\text{n,p})^{97}\text{Nb}$	81.5 ^a	657.9
		$^{98}\text{Mo}(\text{n,np})^{97}\text{Nb}$	12.1 ^a	
		$^{98}\text{Mo}(\text{n,d})^{97}\text{Nb}$	6.3 ^a	

^aincludes contribution from the production and isomeric transition (IT) decay of ^{97m}Nb , but note that different reactions have different probability ratios between ground- and meta-state production (*i.e.* the distribution of production % values for ^{97m}Nb are different to those of ^{97}Nb).

the other hand, the presence of impurity nuclides (not considered in the modelling, but usually unavoidable in experiments) are likely to impact on the measurability of long-lived nuclides and would also need to be considered.

Unfortunately, ^{93}Mo and ^{91}Nb decay predominantly via electron capture, which cannot be easily measured. Meanwhile ^{93m}Nb , which eventually (after 100 years or so) reaches secular equilibrium with ^{93}Mo that decays to it (but is also produced via direct neutron interactions – see table 1), has a very weak gamma emission (at 30.8 keV, $I=5.2\times 10^{-6}$ [56]) that would be challenging to measure. ^{91}Nb very occasionally decays via positron emission (the branching ratio is less than 0.34%) which could be detected from the annihilation signature at 511 keV, potentially using a coincidence counting system (see e.g. [57, 58]) to maximise the measurement sample signal to background ratio. X-ray signatures may be another route to detecting the presence of ^{91}Nb , though may be difficult to interpret unambiguously as to the decay origin. Despite these weak photon emissions, ^{91}Nb was still predicted to be the dominant contributor to γ -dose rate at long cooling times after the DEMO divertor armour operational scenario discussed in section 1.1 (see figure 3(d)).

Once the signals from shorter-lived nuclides in samples have faded (or earlier if those counts do not interfere with the target nuclide’s counts – as in ^{94}Nb) measurements may be more feasible in low background environments via high resolution gamma spectrometry; for example in an underground laboratory such as at the Boulby Underground Science Facility’s ultra-low background materials assay

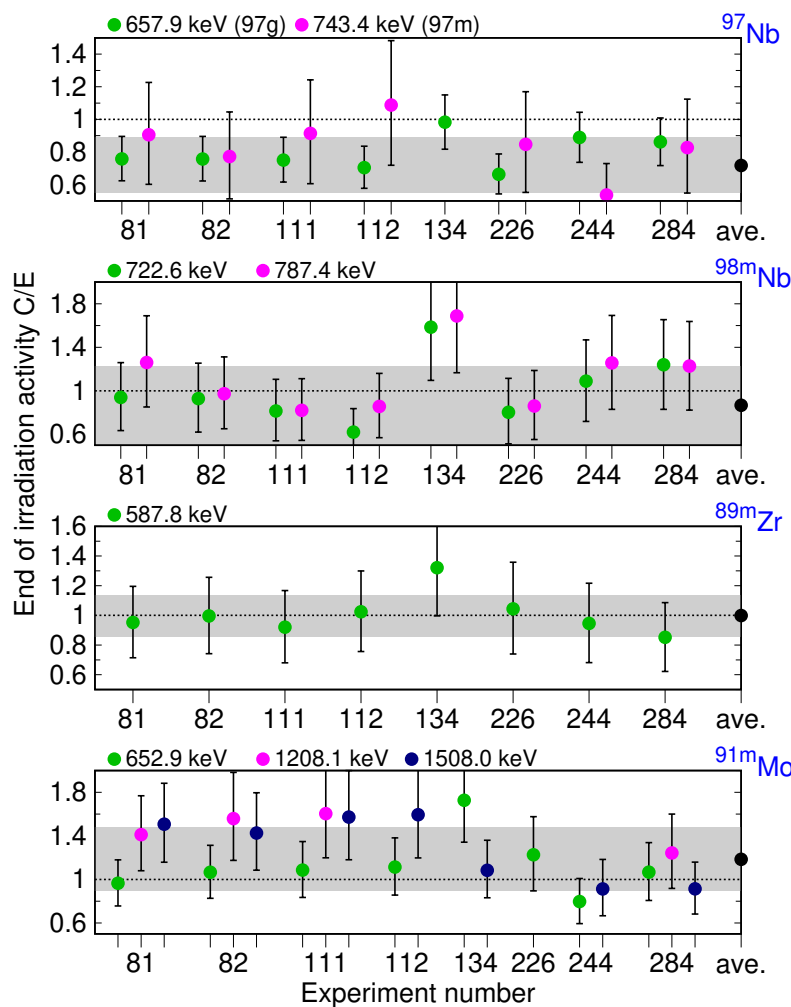


Figure 8. Colour online. The complete set of C/E values calculated for the ASP experiments involving Mo foils. The colour of a point indicates which γ -peak it is associated with (listed at the top of each pane). Points are grouped by experiment along the x-axis. Each pane corresponds to the peaks of a different radionuclide, except for the top pane, where the single measured peaks from each of ^{97}Nb and ^{97m}Nb are shown together. The weighted-average C/E value for all peaks in each pane is also plotted in black, and the grey band behind the data represents the standard deviation of the C/E values from this average. See the main text for details.

infrastructure [59] or using a low background shield with a Compton suppression system in an “above ground” system. An example of the latter (figure 9, below) is available at UKAEA’s ADRIANA laboratory. The detector itself is comprised of a broad energy germanium detector (BEGe), high energy-resolution gamma spectrometer and an array of seven NaI detectors which are used to veto events, reducing the Compton background, and thus improving the detection limits for some

nuclides. Alternatively to gamma spectrometry, low background beta counters or liquid scintillation counting systems may be used to measure some nuclides, such as ^{99}Tc .

A range of complementary techniques may also be needed to enable measurement, spanning radiometric and atom-based diagnostics. The long half-lives of these important radionuclides make them particularly suitable for measurement via Inductively Coupled Plasma Mass Spectrometry (ICP-MS) or Accelerator Mass Spectroscopy (AMS) techniques [60, 61, 62, 63]. However, with such techniques the presence of the bulk material and associated impurity ions, specifically their charge-to-mass ratios (and potentially polyatomic impurity ions formed with e.g Ar plasma), need to be considered for determining the analyte ion detection limits. A mass-based detection technique may offer superior detection limits to nuclear methods with a potential advantage of enabling more rapid assay times in comparison to radiometric approaches, although suitable radiochemistry and tracers may need using in combination with such techniques [61]. Some work has been performed exploring isobaric or isotopic dilution techniques in connection with ICP-MS [61] for ^{99}Tc for example (another one of the less dominant, but still significant nuclides noted in figure 3).

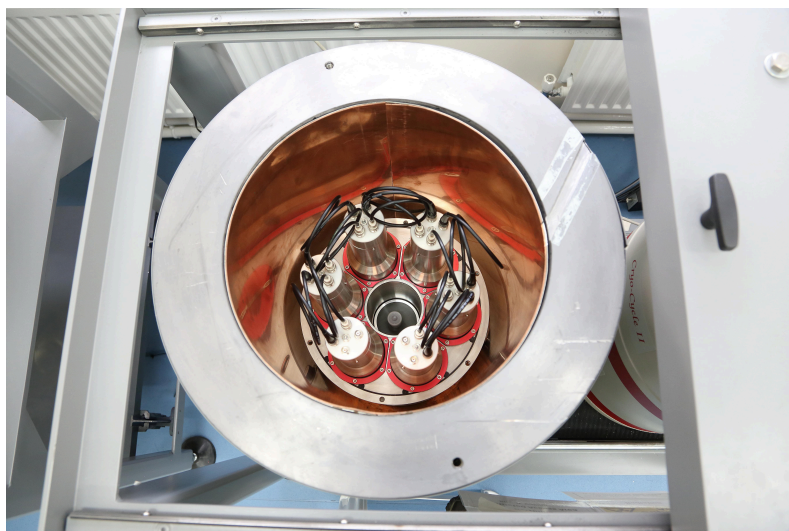


Figure 9. Colour online. Photo shows a Broad Energy Germanium (BEGe) detector with a NaI-based Compton Suppression system. The system sits inside a low background lead housing with additional Sn and Cu layers to reduce Pb x-ray contributions to the background.

5. Conclusions

Inventory calculations with FISPACT-II have highlighted the issues surrounding long-term high-activation of molybdenum if it were to be used as an armour material in fusion systems. However, the simulations predicted that specific stable isotopes (^{96}Mo and ^{97}Mo) from Mo's wide distribution are potentially more favourable, provided the necessary isotopic separation is economically and environmentally advantageous,

compared to the waste handling costs of using standard or natural Mo, or the cost of reduced component lifetime if tungsten (W) remains the default choice.

In parallel, it is important to have confidence in these simulated radiological responses, especially if they are going to be used – in the case of Mo – to make potentially expensive engineering design decisions for future fusion experiments and prototype power plants. Two experimental validation efforts for nuclear inventory code predictions of 14 MeV-neutron-induced activity in Mo have shown that the simulation methodology (FISPACT-II) and underlying nuclear data are reasonably successful. Using several international nuclear data libraries, FISPACT-II was able to accurately simulate decay-heat measurements obtained for Mo after exposure to 14 MeV neutrons for either 5-minutes or seven-hours in JAEA’s defunct FNS facility. Additionally, γ -spectroscopy-derived activation estimates for radionuclides produced in Mo foils irradiated at the ASP 14 MeV-neutron source in the UK have provided a wealth of new data to test code predictions against. For Mo, eight separate experiments were used to derive end-of-irradiation activities for five different radionuclides with detectable γ -emissions. Comparison to simulations of the experiment, performed by FISPACT-II [21] with the TENDL-2017 [22] library, revealed a good agreement (C/E values near to one) despite the large degree of experimental uncertainty and statistical scatter.

While these two benchmarks have helped to improve confidence in some aspects of code predictions for Mo in a fusion environment, further validation is required, particularly for the production rates of the long-lived radionuclides expected to dominate in Mo after exposure to typical demonstration fusion-reactor (DEMO) conditions; ^{91}Nb , ^{93}Mo , and ^{93m}Nb , in particular. The short irradiation timescales associated with the experiments prevent detailed interrogation and testing of the production routes of these long-lived radionuclides. Further experiments, involving longer irradiation and/or higher neutron fluences, are required, potentially in combination with alternative measurement techniques, such as mass spectroscopy, to enable measurement of the radionuclides important for the long-term activation of Mo (not all of which produce measurable γ signals).

At facilities like ASP, there is some scope to perform further experiments involving larger samples exposed to longer irradiations at lower fluxes (e.g. as parasitic experiments added to other campaigns) and, if appropriate, followed by longer γ -spectroscopy measurements in low-background conditions taken at intermittent intervals over the course of several months. Then there is a chance that weak, but relatively constant γ -signals from long-lived nuclides could be observed and used to evaluate some of the important cross sections; not only for Mo, but also for other materials relevant to fusion reactor applications.

However, such experiments are more difficult to arrange (*i.e.* to get sufficient beam-time) and analyse; they would likely have complex irradiation conditions with varying fluxes and breaks in operation, leading to greater uncertainties. There are several proposals being developed around the world to provide more favourable experimental conditions (e.g. IFMIF-DONES [64]); none of the currently available devices have the necessary neutron fluxes, neutron energies or experimental availability to meet the needs of fusion as it moves away from a research focus to a more engineering realisation phase with DEMO and the other near-commercial devices planned.

Despite the above caveats, the present work nonetheless increases confidence in the nuclear code predictions of inventory evolution in molybdenum, which will help to qualify and confirm its viability (or not) as a candidate fusion reactor material; either

in pure form or as part of an alloy, and whether it can be used with its natural isotopic abundances or if tailoring is required. These and future experimental validation efforts help to reduce uncertainty and increase confidence in simulated activity (and waste) predictions that explore the benefit and feasibility of isotope tailoring of Mo for fusion applications, making it possible to justify industrial R&D into producing biased molybdenum at the necessary scale for fusion power plants.

6. Acknowledgements

This work was funded by the RCUK Energy Programme [grant number EP/T012250/1]. To obtain further information on the data and models underlying this paper please contact PublicationsManager@ukaea.uk.

References

- [1] Brooks J N, El-Guebaly L, Hassanein A, and Sizyuk T, 2015, *Nucl. Fus.*, **55** 043002 <https://doi.org/10.1088/0029-5515/55/4/043002>
- [2] Gilbert M R, Packer L W, Sublet J, and Forrest R A, 2014, *Nucl. Sci. Eng.*, **177** 291–306 <https://doi.org/10.13182/NSE13-76>
- [3] Rieth M, Dudarev S L, Gonzalez de Vicente S M, Aktaa J, Ahlgren T, Antusch S, Armstrong D E J, Balden M, Baluc N, Barthe M F, Basuki W W, Battabyal M, Becquart C S, Blagoeva D, Boldyryeva H, Brinkmann J, Celino M, Ciupinski L, Correia J B, De Backer A, Domain C, Gaganidze E, García-Rosales C, Gibson J, Gilbert M R, Giusepponi S, Gludovatz B, Greuner H, Heinola K, Höschen T, Hoffmann A, Holstein N, Koch F, Krauss W, Li H, Lindig S, Linke J, Linsmeier C, López-Ruiz P, Maier H, Matejicek J, Mishra T P, Muhammed M, Muñoz A, Muzyk M, Nordlund K, Nguyen-Manh D, Opschoor J, Ordás N, Palacios T, Pintsuk G, Pippan R, Reiser J, Riesch J, Roberts S G, Romaner L, Rosiński M, Sanchez M, Schulmeyer W, Traxler H, Ureña A, van der Laan J G, Veleva L, Wahlberg S, Walter M, Weber T, Weitkamp T, Wurster S, Yar M A, You J H, and Zivelonghi A, 2013, *J. Nucl. Mater.*, **432** 482–500 <https://doi.org/10.1016/j.jnucmat.2012.08.018>
- [4] Ueda Y, Schmid K, Balden M, Coenen J W, Loewenhoff T, Ito A, Hasegawa A, Hardie C, Porton M, and Gilbert M R, 2017, *Nucl. Fus.*, **57** 092006 <https://doi.org/10.1088/1741-4326/aa6b60>
- [5] Taylor C N, Yamauchi Y, Shimada M, Oya Y, and Hatano Y, 2017, *Fus. Sci. Tech.*, **71** 491–495 <https://doi.org/10.1080/15361055.2016.1273699>
- [6] Edwards D J, Garner F A, and Gelles D S, 2008, *J. Nucl. Mater.*, **375** 370 – 381 <https://doi.org/10.1016/j.jnucmat.2008.01.014>
- [7] Maier H, Neu R, Greuner H, Böswirth B, Balden M, Lindig S, Matthews G F, Rasinski M, Wienhold P, and Wiltner A, dec 2009, *Physica Scripta*, **T138** 014031 <https://doi.org/10.1088/0031-8949/2009/t138/014031>
- [8] Kim H, Lee H J, and Jang C, 2015, *Fus. Sci. Tech.*, **68** 378–382 <https://doi.org/10.13182/FST14-958>
- [9] Fabritsiev S A, Gosudarenkova V A, Potapova V A, Rybin V V, Kosachev L S, Chakin V P, Pokrovsky A S, and Barabash V R, 1992, *J. Nucl. Mater.*, **191-194** 426 – 429 Fusion Reactor Materials Part A, [https://doi.org/10.1016/S0022-3115\(09\)80080-9](https://doi.org/10.1016/S0022-3115(09)80080-9)
- [10] Garner F A, Greenwood L R, and Edwards D J, 1994, *J. Nucl. Mater.*, **212-215** 426 – 430 [https://doi.org/10.1016/0022-3115\(94\)90098-1](https://doi.org/10.1016/0022-3115(94)90098-1)
- [11] Gilbert M R, Eade T, Bachmann C, Fischer U, and Taylor N P, 2017, *Nucl. Fus.*, **57** 046015 <https://doi.org/10.1088/1741-4326/aa5bd7>
- [12] Gilbert M R, Eade T, Rey T, Vale R, Bachmann C, Fischer U, and Taylor N P, 2019, *Nucl. Fus.*, **59** 076015 <https://doi.org/10.1088/1741-4326/ab154e>
- [13] SOMEYA Y and TOBITA K, 2012, *Plasma Fus. Res.*, **7** 2405066 <https://doi.org/10.1585/pfr.7.2405066>
- [14] Gilbert M R and Sublet J -Ch, Handbook of activation, transmutation, and radiation damage properties of the elements simulated using FISPACT-II & TENDL-2015; Magnetic Fusion Plants, CCFE-R(16)36, UKAEA, 2016 available from <http://fispact.ukaea.uk>
- [15] Strategy for the management of solid low level radioactive waste from the non-nuclear industry in the United Kingdom, , Department of Energy & Climate Change, UK, 2012 Available at <https://www.gov.uk/government/publications/>
- [16] MCNP6 User Manual, Version 2.0, 2017; Edited by C.J. Werner, Los Alamos document number: LA-UR-17-29981, Rev. 0. Further details at <http://mcnp.lanl.gov/>
- [17] Fischer U, Bachmann C, Catalan J P, Eade T, Flammini D, Gilbert M R, Jaboulay J -Ch, , Konobeev A, Leichtle D, Lu L, Malouch F, Moro F, Pereslavitsev P, Qiu Y, Sanz J, Sauvan P, Stankunas G, , Travleev A, Turner A, Ogando F, Palermo I, and Villari R, 2017, *Fus. Eng. Des.*, **123** 26–31 <https://dx.doi.org/10.1016/j.fusengdes.2017.01.053>
- [18] Gilbert M R, Eade T, Bachmann C, Fischer U, and Taylor N P, 2018, *Fus. Eng. Des.*, **136** 42–48 <https://doi.org/10.1016/j.fusengdes.2017.12.019>
- [19] Gilbert M R and Sublet J-Ch, 2011, *Nucl. Fus.*, **51** 043005 <http://dx.doi.org/10.1088/0029-5515/51/4/043005>
- [20] Gilbert M R, Sublet J Ch, and Dudarev S L, 2017, *Nucl. Fus.*, **57** 044002 <https://doi.org/10.1088/1741-4326/aa5e2e>
- [21] Sublet J -Ch, Eastwood J W, Morgan J G, Gilbert M R, Fleming M, and Arter W, 2017, *Nucl. Data Sheets*, **139** 77–137 <http://dx.doi.org/10.1016/j.nds.2017.01.002>
- [22] Koning A J and Rochman D TENDL-2017; Release Date: April 25, 2018. Available from

- https://tendl.web.psi.ch/tendl_2017/tendl2017.html
- [23] Harman J, DEMO Operational Concept Description, report number: 2LCY7A, EUROfusion/EFDA, 2012
- [24] Stainer T, Gilbert M R, Packer L W, Lilley S, Gopakumar V, and Wilson C, 2020 Proceedings of the conference of the Physics of Reactors (PHYSOR). <https://www.physor2020.com>
- [25] Eade T, Colling B, Naish J, Packer L W, and Valentine A, apr 2020, *Nucl. Fus.*, **60** 056024
- [26] The Ionising Radiations Regulations, SI 2017/1075, UK Government, 2017 <https://www.legislation.gov.uk/uksi/2017/1075/contents/made>
- [27] Work with ionising radiation, Ionising Radiations Regulations 2017, Approved Code of Practice and Guidance, L121, Health and Safety Executive (HSE), UK, 2018 <https://www.hse.gov.uk/pUbns/priced/l121.pdf>
- [28] Gilbert M R, Fleming M, and Sublet J -Ch, 2017, *EPJ Web Conf.*, **146** 09017 <https://doi.org/10.1051/epjconf/201714609017>
- [29] Fleming M, Stainer T, and Gilbert M R, The FISPACT-II User Manual, UKAEA-R(18)001, UKAEA, 2018 available from <http://fispact.ukaea.uk>
- [30] Smirnov A Y, Bonarev A K, Sulaberidze G A, Borisevich V D, Kulikov G G, and Shmelev A N, 2015, *Physics Procedia*, **72** 126 – 131 Conference of Physics of Nonequilibrium Atomic Systems and Composites, PNASC 2015, 18-20 February 2015 and Conference of Heterostructures for Microwave, Power and Optoelectronics: Physics, Technology and Devices, 19 February 2015. <https://doi.org/10.1016/j.phpro.2015.09.034>
- [31] Noda T, Suzuki H, Araki H, Lyman J L, and Newnam B E, 2002, *J. Nucl. Mater.*, **307-311** 715 – 718 [https://doi.org/10.1016/S0022-3115\(02\)01265-5](https://doi.org/10.1016/S0022-3115(02)01265-5)
- [32] Martynenko Y V, dec 2009, *Physics-Uspokhi*, **52** 1266–1272 <https://doi.org/10.3367/ufne.0179.200912n.1354>
- [33] Smith M L 6 - ELECTROMAGNETIC ENRICHMENT OF STABLE ISOTOPES In FRISCH O R, editor, *Progress in Nuclear Physics*, volume 6 of *The Leading International Review Series in Nuclear Physics*, pages 162 – 191 (Pergamon), 2013 <https://doi.org/10.1016/B978-1-4831-9887-3.50010-4>
- [34] Morgan L W G, Shimwell J, and Gilbert M R, 2015, *Fus. Eng. Des.*, **90** 79 – 87 <https://doi.org/10.1016/j.fusengdes.2014.11.016>
- [35] Shmelev A N and Kozhahmet B K, 2017, *J. Phys.: Conf. Series*, **781** 012022 <https://doi.org/10.1088/1742-6596/781/1/012022>
- [36] Hernández F and Pereslavl'tsev P, 2018, *Fus. Eng. Des.*, **137** 243 – 256 <https://doi.org/10.1016/j.fusengdes.2018.09.014>
- [37] Fleming M, Sublet J -Ch, Gilbert M R, Koning A, and Rochman D, 2017, *EPJ Web Conf.*, **146** 02033 ND 2016: International Conference on Nuclear Data for Science and Technology. <https://dx.doi.org/10.1051/epjconf/201714602033>
- [38] Mosteller R D, Bibliography of MCNP Verification and Validation: 1990 - 2003, LA-UR-03-9032, LANL, 2003 available as https://mcnp.lanl.gov/pdf_files/la-ur-03-9032.pdf
- [39] Maekawa F and Ikeda Y, 2000, *Fus. Eng. Des.*, **47** 377–388 [https://doi.org/10.1016/S0920-3796\(99\)00079-4](https://doi.org/10.1016/S0920-3796(99)00079-4)
- [40] Maekawa F, Shibata Kichiro, Wada M, Ikeda Y, and Takeuchi H, 2002, *J. Nucl. Sci. Tech.*, **39** 990–993 <https://doi.org/10.1080/00223131.2002.10875267>
- [41] Maekawa et al. F, Data collection of fusion neutronics benchmarking experiment conducted at FNS/ JAERI, JAERI-Data/Code 98-021, JAEA, 1998 <http://www.jaea.go.jp/jaeri/>
- [42] Maekawa et al. F, Compilation of benchmark results for fusion related nuclear data, JAERI-Data/Code 98-024, JAEA, 1998 <http://www.jaea.go.jp/jaeri/>
- [43] Maekawa F, Wada M, and Ikeda Y, Decay Heat Experiment and Validation of calculation code systems for fusion reactor, JAERI 99-055, JAEA, 1999 <http://www.jaea.go.jp/jaeri/>
- [44] Gilbert M R and Sublet J, 2019, *Nuclear Fusion*, **59** 086045 <https://doi.org/10.1088/1741-4326/ab278a>
- [45] Gilbert M R and Sublet J -Ch, Fusion decay heat validation, FISPACT-II & TENDL-2017, EAF2010, ENDF/B-VIII.0, JEFF-3.3, and IRDFF-1.05 nuclear data libraries, CCFE-R(18)002, UKAEA, 2018 available from <http://fispact.ukaea.uk>
- [46] Gilbert M R, Packer L W, and Lilley S, 2014, *Nucl. Data Sheets*, **119** 401–403 <https://doi.org/10.1016/j.nds.2014.08.112>
- [47] Packer L W, Angelone M, Gilbert M R, Loreti S, Nobs C R, Pillon M, Sublet J -Ch., and Vilkhivskaya O, 2020 Proceedings of the conference of the Physics of Reactors (PHYSOR) <https://www.physor2020.com>
- [48] Packer L W, Gilbert M R, Hughes S, Lilley S, Pampin R, and Sublet J -Ch, 2012, *Fus. Eng. Des.*, **87** 662–666 Tenth International Symposium on Fusion Nuclear Technology (ISFNT-10).

- <https://doi.org/10.1016/j.fusengdes.2012.01.044>
- [49] Packer L W, Hughes S, Gilbert M R, Lilley S, and Pampin R, 2013, *Fus. Eng. Des.*, **88** 2617–2620 Proceedings of the 27th Symposium On Fusion Technology (SOFT-27); Liège, Belgium, September 24–28, 2012 <https://doi.org/10.1016/j.fusengdes.2013.05.108>
- [50] Lilley S, Packer L W, Pampin R, and Gilbert M R, 2013, *Fus. Eng. Des.*, **88** 2627 – 2630 Proceedings of the 27th Symposium On Fusion Technology (SOFT-27); Liège, Belgium, September 24–28, 2012. <https://doi.org/10.1016/j.fusengdes.2013.05.089>
- [51] Packer L W, Gilbert M R, and Lilley S, 2014, *Nucl. Data Sheets*, **119** 173 – 175 <https://doi.org/10.1016/j.nds.2014.08.048>
- [52] Forrest R A, 2006, *Fus. Eng. Des.*, **81** 2143–2156 <https://doi.org/10.1016/j.fusengdes.2006.01.001>
- [53] Forrest R A, 2011, *Ene. Procedia*, **7** 540–552 Asian Nuclear Prospects 2010, <https://doi.org/10.1016/j.egypro.2011.06.075>
- [54] Krane K S, 1988, *Introductory Nuclear Physics* (John Wiley & Sons, New York, US)
- [55] EXFOR: Experimental Nuclear Reaction Data, www.nds.iaea.org/exfor/
- [56] Live Chart of Nuclides: nuclear structure and decay data; <https://nds.iaea.org/relnsd/vcharthtml/VChartHTML.html>. Based on the Evaluated Nuclear Structure Data Files (ENSDF) (March 2018 snapshot) <http://www.nndc.bnl.gov/ensdf/>
- [57] Davies A V, Burnett J L, and Britton R, 2020, *Nucl. Instrum. Methods Phys. Res., Sect. A*, **951** 163009 <https://doi.org/10.1016/j.nima.2019.163009>
- [58] Britton R, Jackson M J, and Davies A V, 2015, *J. Environ. Radioact.*, **149** 158 – 163 <https://doi.org/10.1016/j.jenvrad.2015.07.025>
- [59] Boulby Underground Germanium Suite (BUGS) - Ultra-low Background Assay; Boulby Underground Laboratory, UK Science & Technology Facilities Council (STFC). <https://www.boulby.stfc.ac.uk/Pages/Ultra-low%20Background%20Material%20Screening.aspx>
- [60] Becker J S, 2003, *Spectrochim. Acta, Part B*, **58** 1757 – 1784 [https://doi.org/10.1016/S0584-8547\(03\)00156-3](https://doi.org/10.1016/S0584-8547(03)00156-3)
- [61] Clases D, Birka M, Sperling M, Faust A, and Karst U, 2017, *J. Trace Elem. Med. Biol.*, **40** 97 – 103 <https://doi.org/10.1016/j.jtemb.2017.01.002>
- [62] Kučera J, Kameník J, Povinec P P, Krausová I, Světlík I, and Fikrle M, 2019, pages 46 – 49 Proceedings of the 5th International Conference on Environmental Radioactivity ENVIRA 2019: Variations of Environmental Radionuclides 8-13 September 2019, Praha, Czech Republic. <https://doi.org/10.14311/ENVIRA.2019>
- [63] Povinec P P, 2017, *Appl. Radiat. Isot.*, **126** 26 – 30 Proceedings of the 7th International Conference on Radionuclide Metrology – Low-Level Radioactivity Measurement Techniques. <https://doi.org/10.1016/j.apradiso.2017.01.029>
- [64] Ibarra A, Arbeiter F, Bernardi D, Cappelli M, García A, Heidinger R, Krolas W, Fischer U, Martín-Fuertes F, Micciché G, Muñoz A, Nitti F S, Pérez M, Pinna T, and Tian K, 2018, *Nucl. Fus.*, **58** 105002 <https://doi.org/10.1088/1741-4326/aad91f>

Appendix A. Reaction cross section graphs

Figure A1 compares TENDL-2017 [22] cross sections to the international database of differential cross section data, EXFOR [4], for the reactions predicted by FISPACT-II to be responsible for the majority (see table 4) of the production of each of the four radionuclides detected in the ASP experiments on Mo. Curves of total cross sections, and the partials to ground and metastable states of each daughter nuclide are shown, and the EXFOR data is also separated by daughter state, subject to the data files from EXFOR containing enough data to make that determination (otherwise the default is “total”).

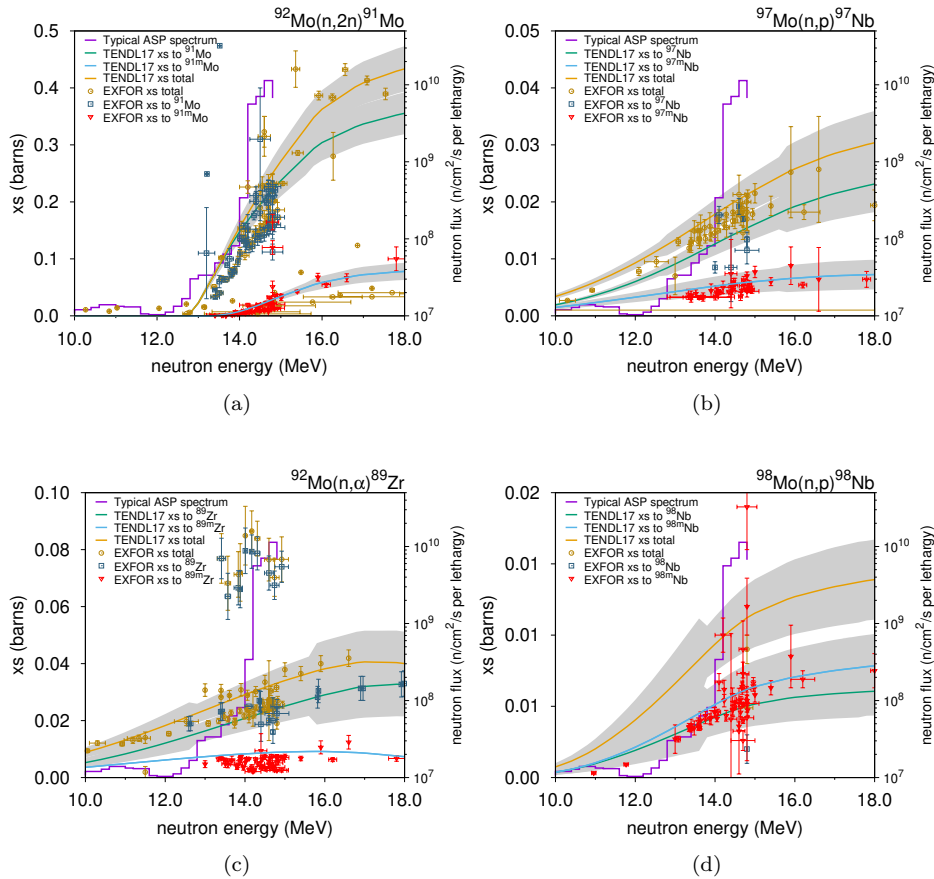


Figure A1. TENDL-2017 reaction cross sections and EXFOR differential data for the main reactions analyzed by the ASP experiments on Mo. TENDL-2017 curves are accompanied by their corresponding uncertainty bands (in grey).